



Design and Optimization of a Surface-Mounted Permanent-Magnet Linear Synchronous Motor with Maxwell ANSYS

Jamal Abdul-Kareem Mohammed*

Farag Mahel Mohammed**

Raghda'a Ahmed A. Ali***

*, **, ***Department of Electromechanical Engineering/ University of Technology/ Baghdad/ Iraq

*Email: 50128@uotechnology.edu.iq

**Email: drfaragmahel@yahoo.com

***Email: gadaahmad460@yahoo.com

(Received 1 August 2018; accepted 28 January 2019)

<https://doi.org/10.22153/kej.2019.01.005>

Abstract

Linear motor offers several features in many applications that require linear motion. Nevertheless, the presence of cogging force can deteriorate the thrust of a permanent magnet linear motor. Using several methodologies, a design of synchronous single sided linear iron-core motor was proposed. According to exact formulas with surface-mounted magnets and concentrated winding specification, which are relying on geometrical parameters. Two-dimensional performance analysis of the designed model and its multi-objective optimization were accomplished as a method to reduce the motor cogging force using MAXWELL ANSYS. The optimum model design results showed that the maximum force ripple was approximately reduced by 81.24% compared to the original model with a smaller ripple coefficient of 0.22. Likewise, the model was redesigned taking into consideration two cases; laminated core and solid core. It was found that the error between the analytical and numerical results of the output force did not exceed 0.0967%.

Keywords: ANSYS, cogging force, linear motor, optimal design.

1. Introduction

Permanent magnet linear motors (PMLMs) are used in wide industrial applications; particularly for high positioning accuracy of concerned implementations. The linear motors (LMs) are mainly based on the electromagnetic concept where they deliver direct linear movement without using gears, cams, belts or other mechanical accessories. This is when the mechanical motion synchronizes the magnetic field. The PMLSMs can be classified into categories: flat or tubular, single sided or double sided, slotted or slot-less, air cored or iron-cored, and longitudinal flux or transverse flux. The LM consists of stator and the translator. Since, it can present direct linear motion with no need for any rotation to translation conversion of equipment; this leads to simplifying system structure and

improving system efficiency [1]. On the other hand, the more predominant nonlinear effect of linear motors is force ripples (detent and reluctance forces) [2]. The detent (or cogging) force is generated by the attraction of the magnets to the LM's core. This force is produced even the winding current is absent. The force demonstrates a periodic relationship with regard to the position of the translator relative to the permanent magnets (PMs) mounted on the stator [3]. Moreover, the reluctance force is generated by the mutation in the winding self-inductance with respect to the position between the translator and stator [4, 5]. Hence, the cogging forces generally cause an undesired vibration and noise; depending on the thrust magnitude [6].

In order to minimize the force ripple, different methods in the literature were developed. One of the most effective methods is the arrangements of

the PMs. Thus, it must be optimized to reduce the cogging force, which is more effective than reluctance force as represented by Lim et al. [7]. Also, the method could be conducted by adding some parts as presented by Baker et al. [8]. It's found that adding a Flux Gathering Ring (FGR) to the outer stator teeth of a linear tubular generator could be an effective method to reducing the end effect. Hence, the cogging reduction happens as resultant. Chung et al. [9] proposed designing and analyzing a flux reversal linear synchronous motor (FRLSM). Three various design parameters were investigated and compared in motor characteristics e.g, back-EMF, detent force, normal force, thrust, and phase inductance by using Maxwell ANSYS. The investigation greatly showed low force ripple and good thrust force linearity via PMs' skewing and three-phase sinusoidal control. Cao et al. [10] investigated the effect of some leading design parameters (mover tooth width, the slot open width the width of the slot under PM, mover height and the motor stack length) on the force performance of a complementary and modular linear flux-switching permanent-magnet (LFSPM) motor. That is using finite element method (FEM). Jalal et al. [11] presented the FEA optimization techniques followed by development of a Matlab/Simulink model to investigate the effects of electrical machine inductance and the combined electromagnetic loading of the machine on the resulting force and cogging force. Palomino et al. [12] proposed a technique to combine the FEM and the statistical regression, which permit to implement the optimal skew angle of the PM. That causes a greater reduction of force ripple with the minimum thrust diminution. Ghasime

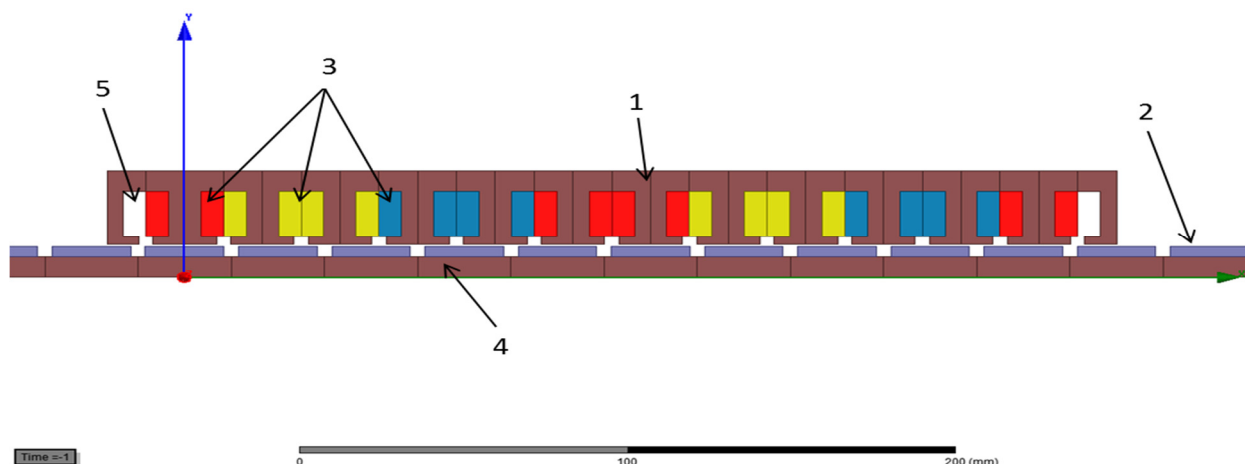
[13] adopted a magnet segmentation method to reduce the cogging torque. Whereas, each surface PM was split into eight parts with symmetrical structure and equal angular widths. The angular gaps between them were utilized for reducing a number of optimization parameters.

Lazov and Uzunov [14] used two methods to reduce the detent force in one innovative PMLSM for 2D laser marking system. Two additional end teeth with chamfers in the magnetic circuit of the movable part were used while the other method modified the teeth of the ferromagnetic core with different lengths.

This paper suggests an optimization method to estimate the optimum dimensions of the PMLSM based on regular steps with the aid of the Maxwell ANSYS simulation. The optimum dimensions required are the magnet length, magnet width, magnet height, air gap length, motor length at z-direction and the motor ends' width.

2. Design Procedure

The PMLSM is a linear motor where the mechanical motion is synchronizing the magnetic field. The PMLSMs can be classified into flat or tubular, single sided or double sided, slotted or slot-less, air cored or iron-cored, and longitudinal flux or transverse flux. In this paper, the design of a single-sided PMLSM with slotted armature core and surface PMs is proposed. A structure model of a three-phase flat type single sided PMLSM according to the MAXWELL ANSYS is depicted as in Fig. (1).



1. Slotted armature core, 2. Surface PMs, 3. Three-phase windings, 4. Yoke, 5. Dummy slot.
Fig. 1. 3D model of the proposed PMSLM.

The core is composed of 13 slots and 13 teeth, 12 slots are filled with single layer concentrated three phase coil windings in a laminated 1010 steel core [15] as a solid core. Each phase in the motor has four slots. These magnetic cores may be made of thin laminations in order to minimize the eddy currents flowing through them. As for all electrical machines, the core losses are composed of hysteresis losses and eddy current losses. The specifications of PMs (NdFeB, Class N42SH) [16] used in the motor design are listed in Table 1.

Table 1,
NdFeB Permanent Magnet Specifications.

B(mT)	H(kA/m)	BH_max(kJ/m ³)	T_max(°C)
1280-1320	>= 1672	320-343	150

Generally, thrust production in the PMLSM is restricted by electrical and magnetic sources. Electrical source depends on the motor coils current. According to Lorentz law [17]:

$$\vec{F} = L\vec{I} \times \vec{B} \quad (\text{vector version}) \text{ and}$$

$$F = IBL \sin\theta \quad (\text{strength only}) \quad \dots(1)$$

at the same time, for magnetic components, the magnetic flux density and inductance effect on the thrust. While the flux of the PMs and coils effect on the magnetic flux density and inductance. This leads to generate a sequence of attracting and repelling forces between the salient poles and the PMs, expressed by a thrust force in the translator [18]. Fig. 2 depicts the working principle of the designed linear motor.

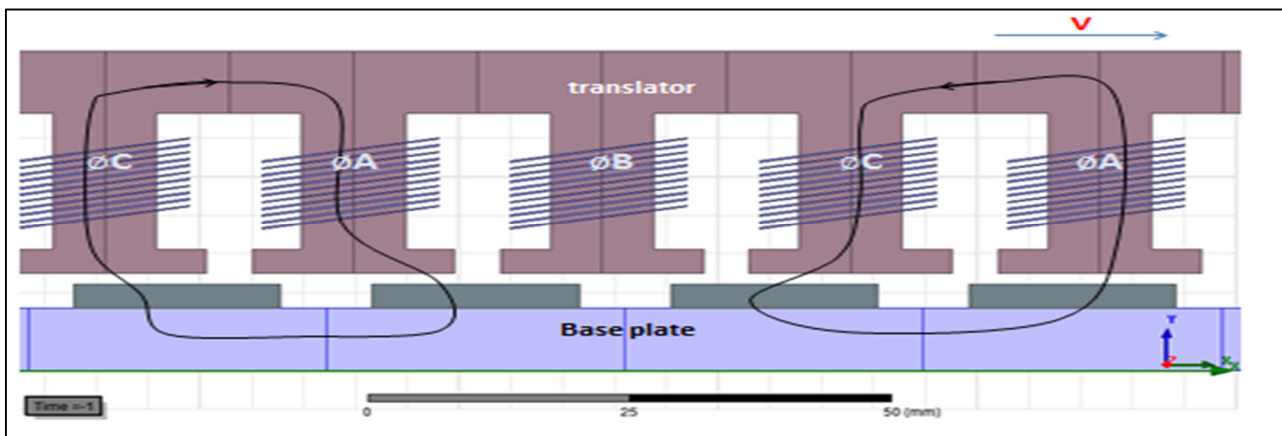


Fig. 2. Working principle of a three-phase PMLSM [19].

As the armature moves, an EMF is induced in the stator windings. By differentiating the PM flux of the phase winding with time, a no-load rms voltage E_f is excited. E_f is excited by the PMs' flux and induced in each phase of the armature winding, it can be given as [17]:

$$E_f = 2\pi f N_1 k_w \Phi_f \quad \dots(2)$$

Where:

$$\Phi_f = \frac{2(F_M - F_{ad} - 4F_{ad}\mathfrak{R}_g/\mathfrak{R}_{lg})/A + 2(F_M + F_{ad}\mathfrak{R}_{lM}/\mathfrak{R}_{lg})(2/\mathfrak{R}_{lM})B}{AC + BD} \quad \dots(3)$$

$$A = 1 + \frac{1}{\mathfrak{R}_{lg}} \left(2\frac{\mathfrak{R}_t}{Q_1} + 0.5\mathfrak{R}_{1c} \right) \quad \dots(4)$$

$$B = 2A\mathfrak{R}_g + 2\frac{\mathfrak{R}_t}{Q_1} + 0.5\mathfrak{R}_{1c} \quad \dots(5)$$

$$C = 2\mathfrak{R}_{PM} + 0.5\mathfrak{R}_{1c} \quad \dots(6)$$

$$D = 1 + 4\frac{\mathfrak{R}_M}{\mathfrak{R}_{lM}} + \frac{\mathfrak{R}_{2c}}{\mathfrak{R}_{lM}} \quad \dots(7)$$

The magnetic circuit of an LSM with surface PMs as illustrated in the equivalent magnetic circuit is shown in Fig. 3.

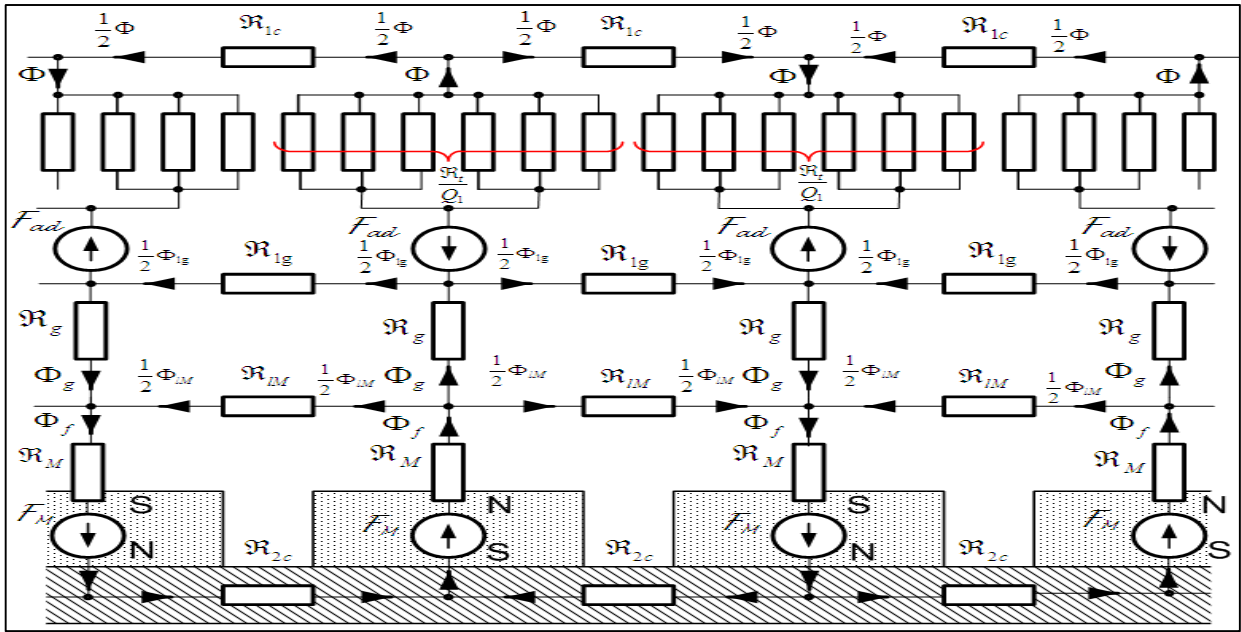


Fig. 3. Equivalent magnetic circuit of a LM with surface PMs [17].

While, the magnetic flux linked with the armature winding may be given as:

$$\Phi = \frac{2(F_M - F_{ad} - 4F_{ad}R_g/R_{1g})D + 2(F_M + F_{ad}R_{IM}/R_{1g})(2/R_{IM})C}{AC + BD} \dots(8)$$

The relation between the velocity and frequency represented by [17]

$$v_s = 2\tau f \dots(9)$$

The frequency could be estimated using Eq. (9), is found to be equal to 17.36Hz. That is according to the parameters listed in Table 2 with the following design parameters:

- $F_{max} = 350N$
- $m_{translator} \approx 6.6kg$
- $m_{load} = 17kg$
- $v_{max} = 1m/s$
- $a_{max} = 1.5m/s^2$

Table 2, LM base line design parameters [20].

L_m (mm)	τ (mm)	ω_p (mm)
288	28.8	24.32

Based on these dimensions and assuming initial teeth lengths and PM volume followed by applying a special algorithm with multiple iterations to obtain the final main design dimensions of the PMs and the geometric dimensions of a single stator slot illustrated in Fig. 4. In the case of using semi-closed slot in the stator core, the detent force depends on the slot aperture width because of the minimizing effect on the slot harmonic components [21].

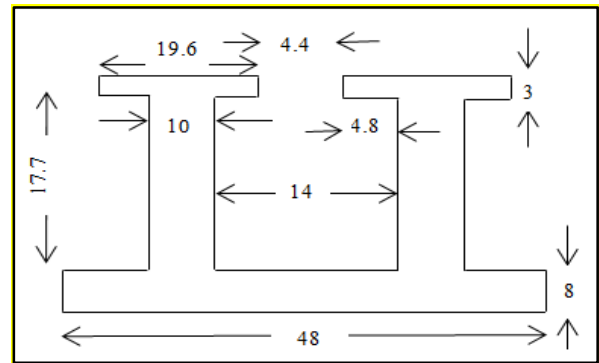


Fig. 4. Dimensions in mm of a single stator slot.

The armature winding resistance as a function of the winding parameters, dimensions, and electric conductivity can be represented by [17]:

$$R_1 = \frac{2(L'_1 K_{1R} + l_{1e}) N_1}{\sigma S_{w1} a_w a_p} \dots(10)$$

In the case of salient pole synchronous motor, the d -axis and q -axis synchronous reactances, respectively can be expressed as:

$$X_{sd} = X_1 + X_{ad} \text{ and } X_{sq} = X_1 + X_{aq} \dots(11)$$

Here, $X_1 = 2\pi f L_1$ is the armature leakage reactance, and X_{ad} and X_{aq} are the d -axis and q -axis armature reaction reactance's, respectively [21] which are calculated as follows:

$$X_{ad} = k_{fd} X_a = 4m_1 \mu_o f \frac{(N_1 k_{w1})^2 \tau L_i}{\pi p g'} k_{fd} \dots(12)$$

$$X_{aq} = k_{fq} X_a = 4m_1 \mu_o f \frac{(N_1 k_{w1})^2 \tau L_i}{\pi p k_c K_{satq} g_q} k_{fq} \dots(13)$$

Where $g' \approx k_c K_{sat} g + h_M / \mu_{rrec}$ is the d -axis equivalent air gap, $K_{sat} > 1$ and $K_{satq} \approx 1$.

Demagnetization curve of the PM is sensitive to temperature changes. Both B_r and H_c reduce as the magnet temperature elevates [17]:

$$B_r = B_{c20} [1 + \frac{\alpha_B}{100} (\theta_{PM} - 20)] \text{ and } H_c = H_{c20} [1 + \frac{\alpha_H}{100} (\theta_{PM} - 20)] \quad \dots(14)$$

Where B_{c20} and H_{c20} are the flux density and coercive force of the PM at 20°C, and $\alpha_B < 0$ and $\alpha_H < 0$ are the temperature coefficients in %/°C for B_r and H_c , respectively. The relative recoil magnetic permeability at PM temperature θ_{PM} of 50°C can be calculated as:

$$\mu_{rrec} = \frac{B_r}{\mu_0 H_c} \quad \dots(15)$$

Where $\mu_{rrec} = 1.161$. The following equations are the rms d -axis and q -axis armature currents as a function of V_1 , X_{sd} , X_{sq} , R_1 , E_f , and δ as shown in Fig. 5.

$$I_{ad} = \frac{V_1(X_{sq} \cos\delta - R_1 \sin\delta) - E_f X_{sq}}{X_{sd} X_{sq} + R_1^2} \text{ and } I_{aq} = \frac{V_1(R_1 \cos\delta - X_{sd} \sin\delta) - E_f R_1}{X_{sd} X_{sq} + R_1^2} \quad \dots(16)$$

$$I_a = \sqrt{I_{ad}^2 + I_{aq}^2} \quad \dots(17)$$

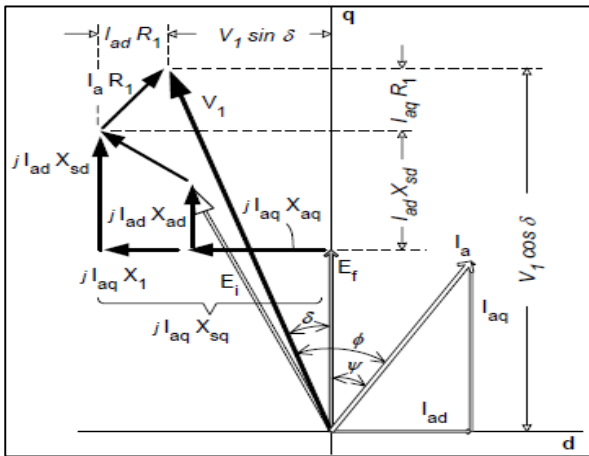


Fig. 5. Full phasor diagram of a LSM [14].

The peak line current density of the armature or the specific electric loading is determined as:

$$A_m = \frac{m_1 \sqrt{2} N_1 I_a}{p\tau} \quad \dots(18)$$

The input power P_i delivered to the armature winding is given by:

$$P_i = m_1 V_1 I_a \cos \phi \quad \dots(19)$$

The copper losses in the core windings is: $P_{\Delta cu} = m_1 I_a^2 R_1$. The electromagnetic power (P_{elm}) and thrust force (F_{dx}), respectively can be given as [17,22]:

$$P_{elm} = \frac{m_1 [V_1 (R_1 \cos\delta + X_{sd} \sin\delta) - E_f R_1]}{(X_{sd} X_{sq} + R_1^2)^2} \times [V_1 (X_{sq} \cos\delta - R_1 \sin\delta) (X_{sd} - X_{sq}) + E_f (X_{sd} X_{sq} + R_1^2) - E_f X_{sq} (X_{sd} - X_{sq})] \quad \dots(20)$$

$$F_{dx} = \frac{P_{elm}}{v_s} \quad \dots(21)$$

So, the force ripple coefficient k_r could be calculated by [23]:

$$k_r = \frac{(F_{max} - F_{min})}{F_{ave}} \quad \dots(22)$$

3. Finite Element Simulation A. Solving and Post-Processing

Finite element method is one of the most accepted and widely used tools for the solution and optimization of linear and nonlinear partial differential equations [24]. In the current work, the analysis was performed using MAXWELL ANSYS that ignored end windings due to using 2D model. The structure parameters of the motor were presented. The solution was divided into two stages, load and no-load transient magnetic solution. Time-stepping FEA method depending on Maxwell equations was applied for analyzing and optimizing the magnetic and force characteristics of the LM. In the process of solving nonlinear transient magnetic problem, the calculated values of voltage V_1 is 45V (at load) and frequency $f= 17.36\text{Hz}$, whereas the solution would be divided into 36 steps with 0.0016sec time period at 0.0001 nonlinear residual using backward Euler time integration method.

Mover mesh of the original motor is illustrated in Fig. 6 where the mesh should be dense enough to minimize the error calculation, whereas the model was designed with three regions of meshing. Each region contains 1200 elements.

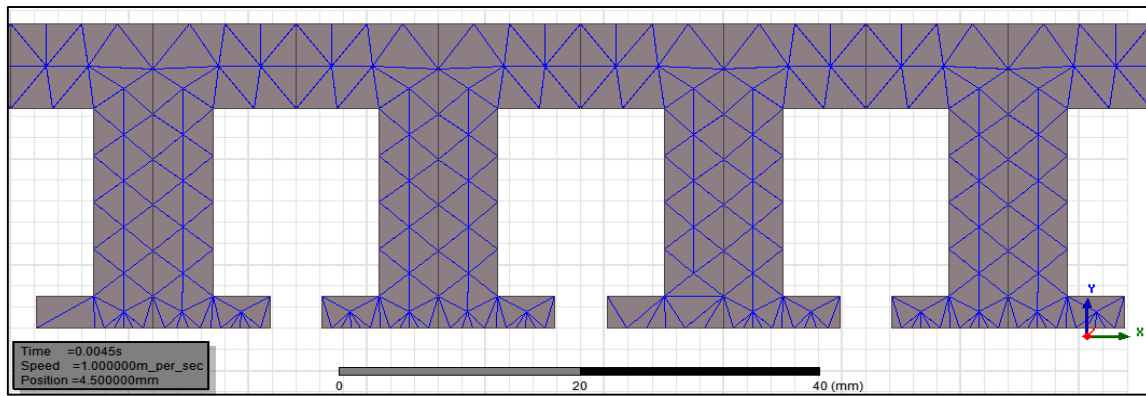


Fig. 6. Mover mesh of one region, 4 slots (x & y are the length and the height of the stack, respectively) at position = 4.5mm with respect to the stator, time = 0.0045 sec from initial position.

B. Magnetic Field Distribution

On no-load case, considering the axial symmetry of the PMLSM, the designed motor was simplified to a 2D axial symmetry model in Cartesian coordinates ignoring core losses. An irregular distribution of the current density in the

conductor was considered. The distribution of the magnetic lines is depicted as shown in Fig. 7. Various shades of rainbow color denoted magnetic flux density values at time equal to 0.0032 sec plus the leakage flux inside the slots was clearly noticed.

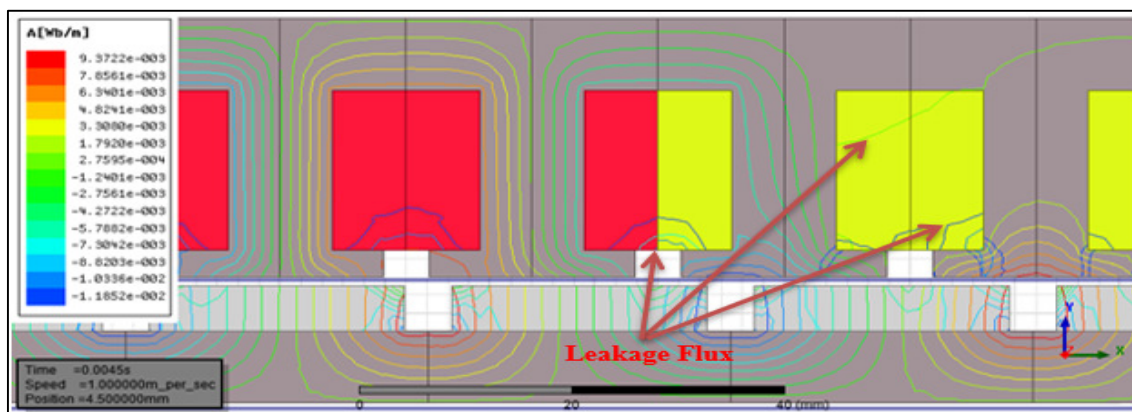


Fig. 7. Distribution of linkage magnetic field lines as closer section with the leakage magnetic field lines (x: motor height, y: reaction rail (yoke) length).

Furthermore, the instantaneous PM flux linkages and induced back *emf* waveforms at no-load magnetic field solutions were obtained as shown in Figs. 8 and 9, respectively. It was observed that the waveform of the flux linkage was approximate sinusoid. Since there was no harmonic magnetic flux, which might be induced

by the current at the load case. The PMs flux waveforms were three phase symmetrical, i.e. they had the same magnitude with 120 electrical degrees shifting. This is a fundamental requirement of three-phase motor design. Unlike the flux linkage, the back *emf* has irregular sinusoid.

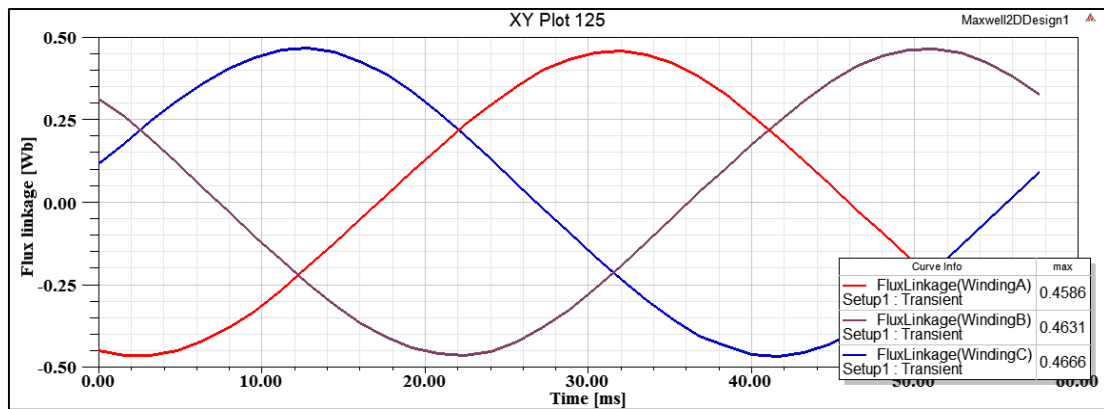


Fig. 8. 3-phase flux linkage waveforms of the original design at no-load case.

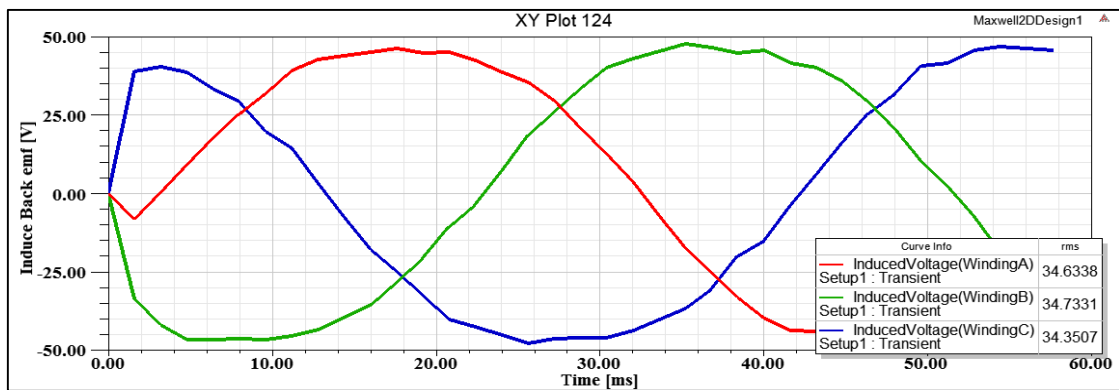


Fig. 9. 3-phase induced back *emf* waveforms of the original design at no-load case.

Figure 8 shows that the maximum value of flux linkage on one coil is $\approx 0.46\text{Wb}$, while the rms value of the back *emf*, E_f is about 34.63V . Considering that the phase winding consisted of one active coil at any instant. The comparison of values above with the analytical calculations where the PM flux was $\Phi_f = 0.4508\text{Wb}$ (Eq. (3))

and the back *emf*, $E_f = 34.3\text{V}$ (Eq. (2)) shows small error between them. Representation of the magnetic field density graph can be illustrated in Fig. 10. It can be noticed that the flux lines move in the transverse direction forming closed loops between each other.

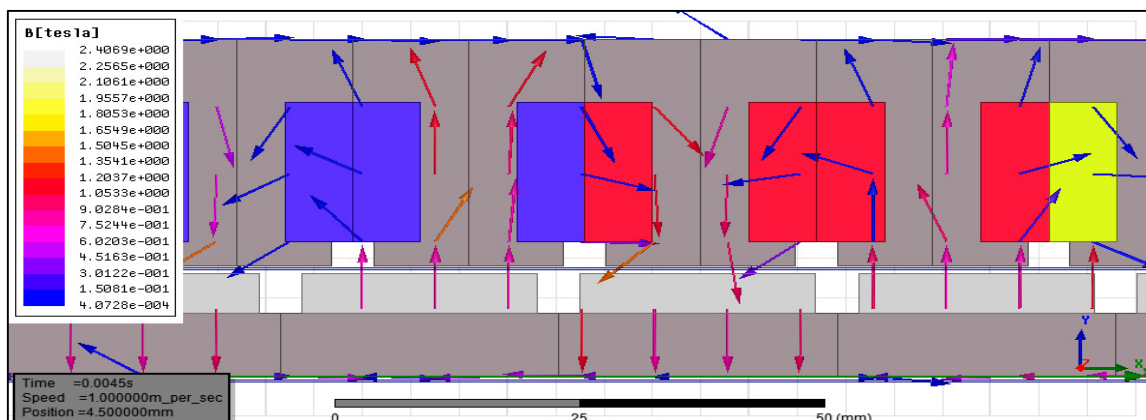


Fig. 10. Magnetic field density as a vector in air-gap, core, back-iron along with magnet at position = 4.5 mm, time = 0.0045sec from initial position.

C. Simulink Design Optimization of the PMLSM Model with and without Core Losses

Figure 11, shows the PMLSM model's thrust force at load moving 2τ distance to $+x$ direction and the armature current waveforms for the original model with three-phase AC voltage

source, neglecting the core losses of the laminated core. The thrust force with rms value was found to be 350.3387N (with 0.9176 ripple coefficient) at $I_a \approx 4.32A$. The thrust ripple depended on the field harmonic produced by the magnets (in the air gap) in addition to current harmonics.

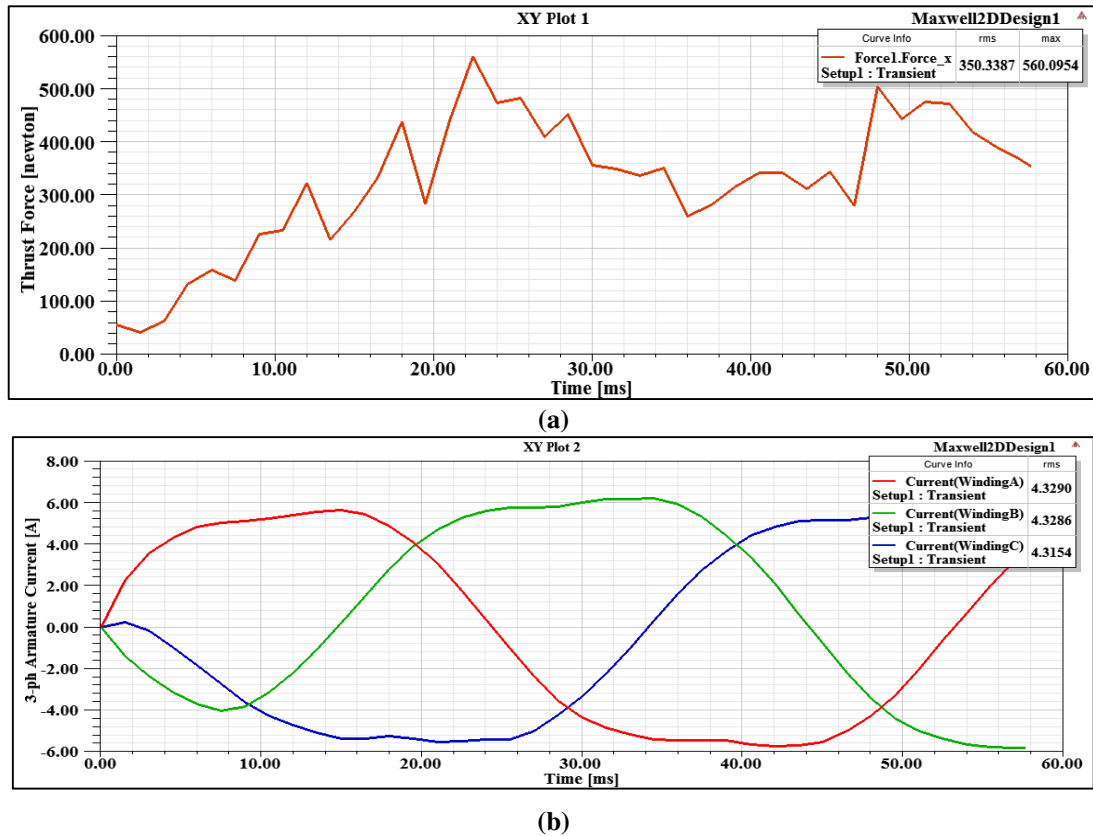


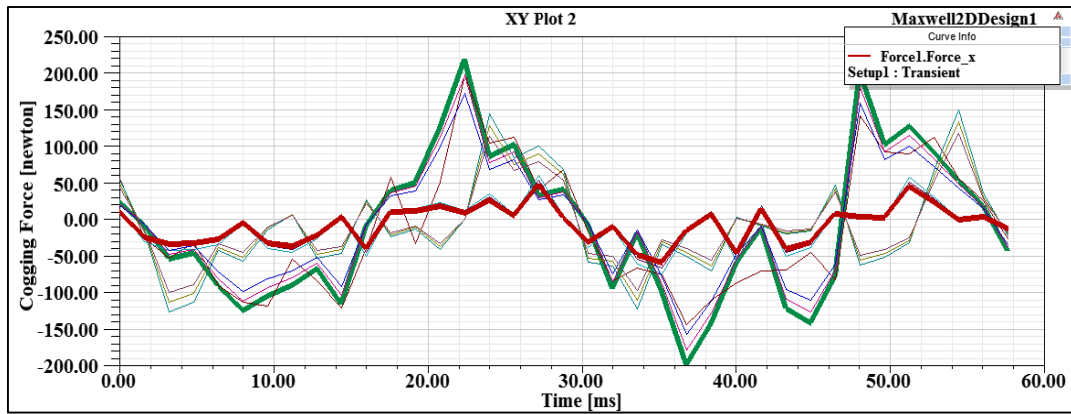
Fig. 11. The simulation results; (a) thrust force,(b): 3-phase currents.

The optimization was accomplished based on the model in Sec. 2. Fig. 12, shows the results of two cases based on MAXWELL ANSYS analysis to predict best dimensions that lead to minimum cogging force at no load case. In Fig. 12-a, the analysis was accomplished based on Table 3-a (first design). the analysis has shown that the maximum cogging force was decreased by 73.9%. Fig. 12-b presents the second design results, which were done with another set of constant values. The cogging force results have decreased by 77.43%.The second design gave the best percentage value of the cogging force reduction.

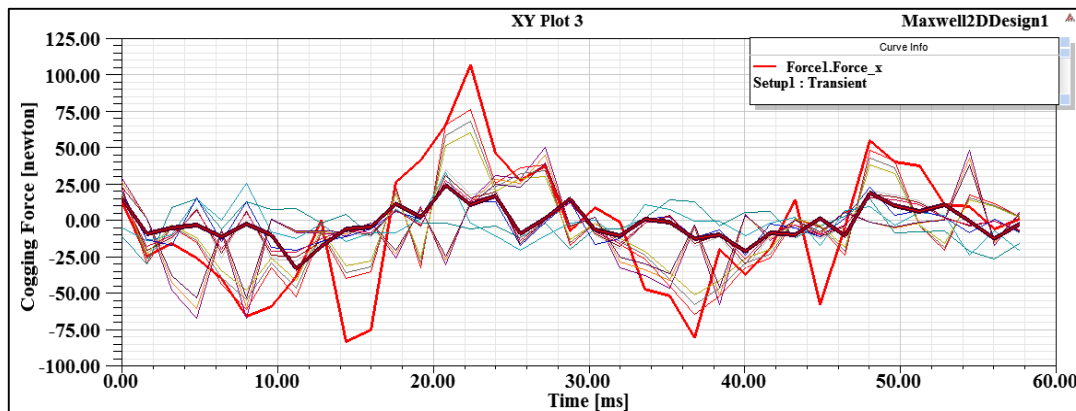
Fig. 12-c represents the ends widths effect on the cogging forces variation of second design at constant values of ($e_m=5$, $g=1.5$ and $h_M=3$) with ends width of Table 3-b. The results showed that, using 2.5mm end length led to 81.24% reduction in cogging force.

Table 3, (a) First case and (b) Second case of optimization procedure (All dimensions in mm).

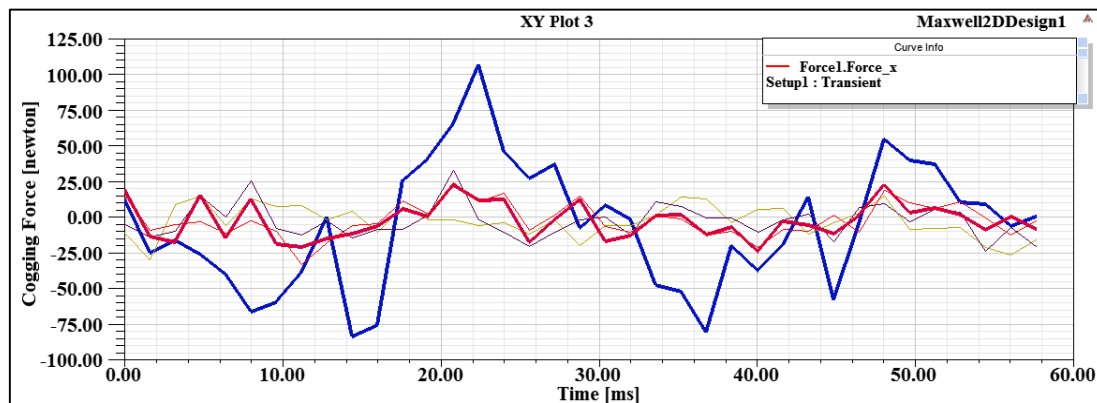
(a)				
Parameters	g_1	h_M	$\omega_p \& L'_1$	
Iterations	First	1	5	
				24.32 - 95
				18.66 - 95
				12.32 - 95
				24.32 - 85
				18.66 - 85
Second	1.5	3	12.32 - 85	
			24.32 - 75	
			18.66 - 75	
			12.32 - 75	
(b)				
One of the ends length e_m (Iterations)	Constant Parameters			
0.25	$g_1 = 1.5$			
1.4375	$h_M = 3$			
2.625	$\omega_p = 12.32$			
3.8125	$L'_1 = 75$			
5	$L_M = L'_1 = 75$			



(a) Cogging forces at constants ($e_m=5, g=1$ & $h_M=5$) mm with different values of ω_p & L'_1 .



(b) Cogging forces at constants ($e_m=5, g=1.5$ & $h_M=3$) mm at different values of ω_p & L'_1 .



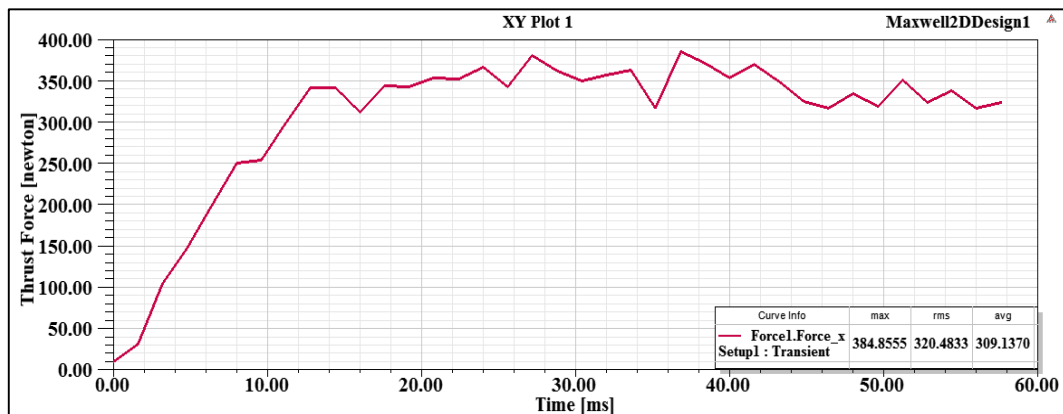
(c) Cogging forces at different ends widths with best dimensions of step (b); ($g=1.5, h_M=3, \omega_p=12.5$ & $L'_1=75$) mm .
 Fig. 12. Best dimensions of the optimum value of the cogging force.

Table 4 clarifies the original model dimensions and parameters plus the optimum design results from the steps above. That is to find the optimum output thrust as illustrated in Fig. 13 for the load case using MAXWELL ANSYS. The rms value of the output force was found to be equal to 320.4833N at the mean value for the rms motor currents of $I_a = 3.555A$. The output force might be equal to 320N at $m_{load} = 17kg$ and optimum

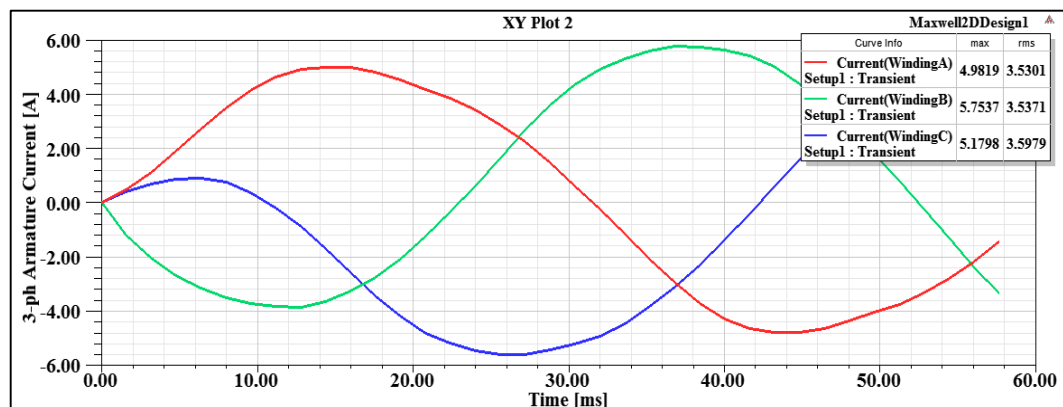
$m_{translator} \approx 4.75kg$. It could be seen that the thrust ripple reduced effectively for the optimal designed motor case. In fact, the optimized motor suffered from thrust ripple twice less than that for the original model. Therefore, the rms input voltage of three phase had to be increased by 11.56V to compensate the lost thrust caused by reducing the PM volume.

Table 4,
The major dimensions and parameters of the two design models; calculated and optimal.

Symbols	Dimensions and parameters	Quantities	
		Calculated	Optimum
P_{in}	Input power (W)	402.7	411.21
V_l	Rated voltage (V)	45	56.568
I_a	Armature current (A)	4.3	3.555
f	Magnetic field frequency	17.36	17.36
N_1	Number of turns of coil winding/phase	280	480
g_l	Air gap length (mm)	1	1.5
e_m	One of the ends length (mm)	5	2.5
R_l	Armature winding resistance/phase (Ω)	0.95	2.48
L_l & L_M	Length of the laminated stack at z direction (mm)	95	75.2
d_w	Diameter of copper wire (mm)	1.3	0.95
ω_p	PM width (mm)	24.32	12.5
h_M	PM height (mm)	5	6
h_{c2}	Stator height (mm)	8	8
X_l	Armature leakage reactance (Ω)	1.8723
X_{ad}	d-axis synchronous reactance (Ω)	1.0228
X_{aq}	q-axis synchronous reactance (Ω)	0.86023
K_w	Winding factor [25]	0.966
Δ	Load angle (degrees)	8.85
ΔP_{cu}	Copper losses (w)	52.7	91.21



(a) Thrust force as a function of time at rms current = 3.555A with optimum parameters.

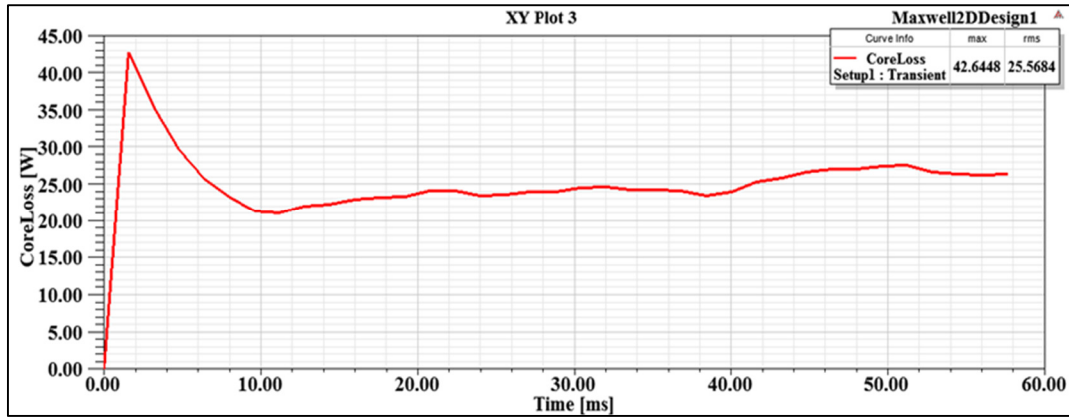


(b) 3-phase of 2D simulated currents with optimum parameters.

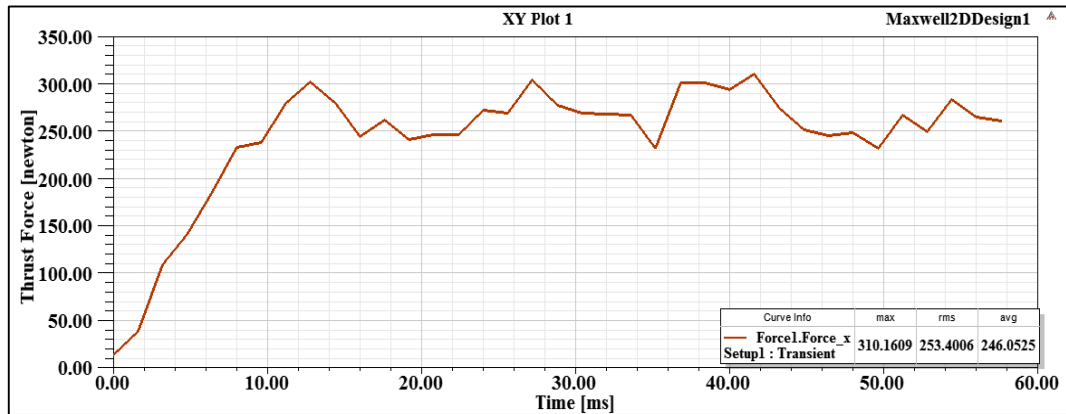
Fig.13. Motor performance with optimum parameters.

The core loss could affect the machine flux linkages. As these measurements were done at low speed, consequently the core loss component was sort of small where it was equal to (25.568W) as shown in Fig. 14-a and the output force at Fig. 14-b was (253.4N) at mean value of the rms

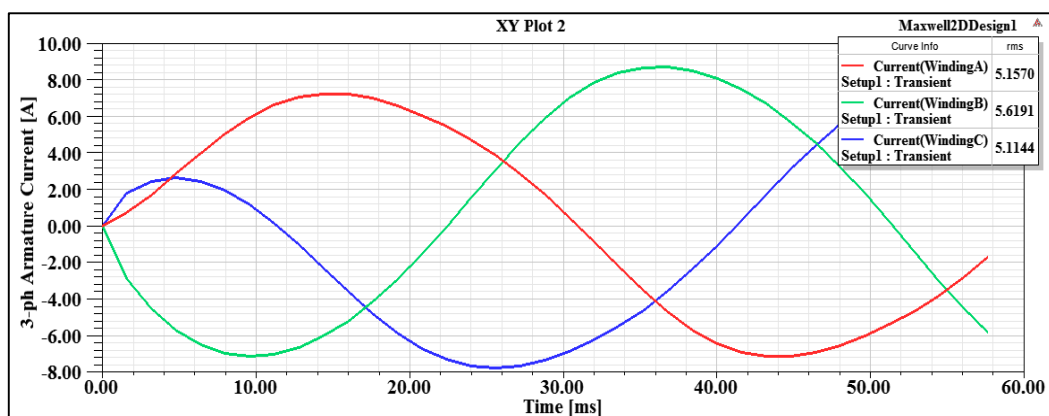
motor currents of $I_a = 5.29$ A. Therefore, errors in the flux linkage computation were small since magnetic losses were caused by harmonic main flux and harmonic leakage flux [26].



(a)



(b)



(c)

Fig. 14. (a) Iron losses of optimum solid core, (b) Output thrust in this case and (c) 3-phase currents.

Thrust force constants, force ripple coefficient and the efficiency percentage [27] results are illustrated in Table. 5. The greater value of the force constant ($k_F = F_{dx} / I_a$) [28] led to least thrust

ripple k_r and highest efficiency which represented the best model. Variant results were observed in the model's k_{F-RMS} values. This disparity was located due to a few reasons whereas two of them

were convergent unlike the rest. The convergence of the first two models' values was related to the error between the exact and the analytical equations. While the increment of the third model was due to applying the optimization method to enhance the performance, which is the goal of this paper. On the other hand, loss consideration in the

fourth model caused the k_{F-RMS} value to decrease. However, the ripple coefficient was equal to 0.319 that was considered an acceptable value to the practical designs in comparison with rest of the models that contain high efficiency or better ripple coefficient but remain a virtual design.

Table 5,
Force constant values, ripple coefficient, and efficiency

models	k_{F-Max} (N/A)	k_{F-Min} (N/A)	k_{F-RMS} (N/A)	I_a (A)	k_r	Efficiency %
1-Analytical model	81.395	4.3	86.91
2-Simulated model	129.65	59.814	81.096	4.32	0.93	86.92
3-Optimal model	108.257	88.963	90.15	3.555	0.22	77.82
4-Optimal model with losses	58.631	43.73	47.845	5.2962	0.319	64

4. Conclusions

Towards enhancing the performance of the single sided PMLSM, a primary structure of 10/12 pole-slot three phase synchronous single-sided linear motor has been designed and modeled using 2D FEA simulation whereas a Maxwell ANSYS has been employed. The following conclusions can be presented:

1. The design achieves optimum motor performance with minimum thrust ripple coefficient of 0.22 and thrust force of 320.4833N at rms load current of 3.555A where k_{F-RMS} of 90.15.
2. The optimized motor gives a thrust ripple twice less compared to the original model.
3. Some loss of thrust force is caused by the reduction in the PMs volume.
4. The core losses are introduced as a second case with a laminated core for the optimum model producing a thrust ripple coefficient of 0.319 and thrust force of 253.4 N at rms load current of 5.2962A where k_{F-RMS} of 47.845.
5. The analytical model and numerical simulations results show a good agreement with maximum error not exceeding 0.0967%.

Notation

A, B, C, D	constants based on magnetic circuit of an LSM with surface PMs
a_{max}	motor acceleration at the starting
a_p	the number of parallel current path
a_w	the number of parallel conductors
B	magnetic field density
BH_max	maximum energy production
F_{ad}	the d -axis armature reaction MMF
F_{ave} , F_{min}	average output thrust and minimum

F_M	thrust, respectively the equivalent MMF produced by one pole of the PM
F_{max} , F_{dx}	thrust force
f	the input motor frequency
g_q	the q -axis air gap length
H	magnetic field strength
h_M	PM height of a single pole
K_{1R}	the skin effect coefficient
K_{sat}	the saturation factor of the magnetic circuit
K_{satq}	the saturation factor in the salient pole excitation system
k_C	the Carter's coefficient for the air gap
k_w	the armature winding coefficient
L'_1	the laminated stack length
L_i	the stator core effective length
L_M	PM Length
L_m	motor length
l_{1e}	the mean length of a single end connection
m_1	the number of motor phases
m_{load}	load mass
$m_{translator}$	translator mass
N_1	the number of stator winding turns
Q_1	the number of slots per pole
\mathcal{R}_{1C}	the reluctance of the armature core (yoke) per pole pitch
\mathcal{R}_{2C}	the reluctance of the reaction rail core (yoke) per pole pitch
\mathcal{R}_g	the reluctance of the air gap
\mathcal{R}_{lg}	the reluctance of the air gap leakage flux
\mathcal{R}_{lm}	the reluctance for the PM leakage flux
\mathcal{R}_{PM}	the reluctance of the PM
\mathcal{R}_t	the reluctance of a single tooth
S_{w1}	the armature conductor cross

	section
T_{max}	maximum working temperature
v_{max}	motor velocity

Greek letters

δ	the load angle between the terminal motor phase voltage V_1 and E_f
Φ_f	the magnetic flux produced by the PM
\emptyset	the motor power factor angle, the phase angle between V_1 and I_a
$\emptyset_A, \emptyset_C,$ \emptyset_B	the magnetic flux of three phases A, B and C, respectively
ω_p	PM width
θ	the angle between the field direction and the conductor direction
μ_o	the free space magnetic permeability
σ	the electric conductivity of a conductor at an operating temperature
τ	pole pitch

5. References

- [1] A. Basak, Permanent-Magnet DC Linear Motors. Oxford, Clarendon Press, 1996.
- [2] G. Otten, Theo J.A. De Vries, A.M. Rankers, E.W. Gaal, "Linear motor motion control using a learning feedforward controller," IEEE/ASME Transactions on Mechatronics, pp.161-70, 1997.
- [3] K.K. Tan, T.H. Lee, H.F. Dou, S.J. Chin and S. Zhao, "Precision Motion Control with Disturbance Observer for Pulsewidth-Modulated-Driven Permanent-Magnet Linear Motors," IEEE Transactions on Magnetics, vol. 39, no. 3, May 2003.
- [4] C. Rohrig, "Identification of Force Functions for Permanent Magnet Linear Synchronous Motors," In Proceedings of The 5th International Symposium on Linear Drives for Industry Applications, LDIA2005, Kobe-Awaji, Japan, September 25-28, 2005. Pp.536-539.
- [5] D. Wu , A. S. Jalal and N. Baker, "A coupled model of the Linear Joule Engine with embedded tubular permanent magnet linear alternator," Energy Procedia vol. 105, PP. 1986 – 1991, 2017.
- [6] I.I. Abdalla, Z.A. Anwarudin, A.R.T. Firmansyah, A.R. A. Aziz and M.R. Heikal, "Cogging Force Issues of Permanent Magnet Linear Generator for Electric Vehicle," J. Electrical Systems, pp. 489-502, 2017.
- [7] K.C. Lim, J.K. Woo, G.H. Kang, J.P. Hong, and G.T. Kim, "Detent Force Minimization Techniques in Permanent Magnet Linear Synchronous Motors", IEEE Transactions on Magnetics, Vol. 38, No. 2, 2002.
- [8] N. J. Baker, R.M. Korbekandi, A. Sa. Jalal and D. Wu, "Performance of a tubular machine driven by an external combustion free piston engine," 9th International Conference on Power Electronics, Machines and Drives (PEMD 2018), Liverpool. UK, 2018.
- [9] S.U. Chung, H.J. Lee, and S.M. Hwan, "A Novel Design of Linear Synchronous Motor Using FRM Topology," IEEE Transactions on Magnetics, vol. 44, no. 6, Jun.2008.
- [10] R. Cao, M. Cheng, C.C. Mi and W. Hua, "Influence of Leading Design Parameters on the Force Performance of a Complementary and Modular Linear Flux-Switching Permanent-Magnet Motor," IEEE Transactions on Industrial Electronics, vol. 61, no. 5, pp. 2165-2175,2014
- [11] A. S. Jalal, N. J. Baker and D. Wu, "Electrical Machine Design for use in an External Combustion Free Piston Engine,"5th IET International Conference on Renewable Power Generation (RPG). London, UK, pp. 1-6, 2016.
- [12] G.G. Palomino, J.R. Conde and E. Laniado, "Optimization of Permanent Magnet Skew in Permanent Magnet Linear Synchronous Motors Using Finite Element and Statistical Method," Engineering, pp. 577-582, 2011.
- [13] A. Ghasime, "Cogging Torque Reduction and Optimization in Surface-mounted Permanent Magnet Motor Using Magnet Segmentation Method," Electric Power Components and Systems, vol. 42, no. 12, pp. 1239- 1248, 2014.
- [14] L. Lazov and p. Uzunov, "Minimizing the Detent Force in Permanent Magnet Linear Synchronous Motor for driving of 2D Laser Marking Table," In Environment Technology and Resources: Proceedings of the11th International Scientific and Practical Conference, vol. 3, Rezekne, Latvia 2017, pp. 174-178.
- [15] AISI 1010 Steel Data Sheet, Authorized Precision Ball and Roller Distributors in the UK, Available on: <https://simplybearings.co.uk/shop/files/1010.pdf>
- [16] Sintered Neodymium Iron Boron (NdFeB) Magnets – Eclipse Magnetics, Available on:

- https://www.eclipsemagnetics.com/media/wysiwyg/brochures/neodymium_grades_data.pdf
- [17] J.F. Gieras, Z.J. Piech, B.Z. Tomczuk, Linear Synchronous Motor-Transportation and Automation Systems, 2nd Edition, CRC Press, Taylor & Francis, Florida, 2000.
- [18] S.A. Nasar and I. Boldea, Linear Electric Motors: Theory, Design and Practical Applications, 1st Edition, Prentice-Hall, 1987.
- [19] G. Otten, T. J.A. de Vries, J. v. Amerongen, A. M. Rankers, and E. W. Gaal, "Linear Motor Motion Control Using a Learning Feedforward Controller," IEEE/ASME TRANSACTIONS ON MECHATRONICS, vol. 2, no. 3, pp. 1083–4435, September 1997.
- [20] X. Wang, P. Wang and X.Xu, "Magnetic Field Analytical Calculation of the Permanent Magnet Synchronous Linear Motor with Fractional Slot Concentrated Windings," In proceedings of 17th International Conference on Electrical Machines and Systems, ICEMS2014, Hangzhou, China, Oct. 22-25, 2014.
- [21] K.C. Lim, J.K. Woo, G.H. Kang, J.P. Hong and G.T. Kim, "Detent Force Minimization Techniques in Permanent Magnet Linear Synchronous Motors," IEEE Transactions on Magnetics, vol. 38, no. 2, 2002.
- [22] H.A. Toliyat and G.B. Kliman, Handbook of Electric Motors, 2nd Edition, Taylor & Francis Group, LLC, 2004.
- [23] A. L. Shurajji, Z.Q. Zhu, and Q.F. Lu, "A Novel Partitioned Stator Flux Reversal Permanent Magnet Linear Machine", In proceedings of 2015 Tenth International Conference on Ecological Vehicles and Renewable Energies (EVER), 2015.
- [24] F. Al-Shamma, F. F. Mustafa and S. M. Saliman, "An Optimum Design of Cam Mechanisms with Roller Follower for Combined Effect of Impact and High Contact Loads," Al-Khwarizmi Engineering Journal, vol. 6, no. 4, pp. 62 – 71, 2010.
- [25] C. Svihus, Investigation of Interior Permanent Magnet Machines with Concentrated Windings for High Dynamics Applications, MSc. Thesis, Christian Sihus Spring 2015.
- [26] A.M. Saleh and A.Th. Radhi, "EFFECT OF HARMONICS ON A SOLID-ROTOR INDUCTION MOTOR," Journal of Engineering, vol. 12, no. 1, pp. 199-217, march, 2006.
- [27] A.S.J. Abdi, "Steady State Performance Investigation of a Three Phase Induction Motor Running Off Unbalanced Supply Voltages," Al-Khwarizmi Engineering Journal, vol. 7, no. 3, pp. 1 – 12, 2011.
- [28] Q. Lu, J. Shi, X. Huang, Y. Fang and Y. Ye, "Performance of Partitioned Primary Linear Switched Flux PM Machines," IEEE, pp.2486-2491, 2016.

تصميم وتحقيق التصميم الامثل للمحرك الخطي التزامني ذو المغناطيس الدائم المثبت على السطح باستخدام برامج ماكسويل أنسرز

جمال عبد الكريم محمد* فرج محل محمد** رгдаء أحمد عبد علي***

***،**،* قسم الهندسة الكهروميكانيكية / الجامعة التكنولوجية / بغداد/ العراق

* البريد الالكتروني: 50128@uotechnology.edu.iq

** البريد الالكتروني: dfaragmahel@yahoo.com

*** البريد الالكتروني: gadaahmad460@yahoo.com

الخلاصة

يوفر المحرك الخطي العديد من المميزات في العديد من التطبيقات التي تتطلب حركة خطية. على الرغم من ذلك، فإن وجود قوة التجاذب المغناطيسي التي تشابه قوى الترس الميكانيكية يمكن أن يتسبب في تدهور قوة الدفع في محرك خطي ذي مغناطيسي دائم. لذلك تم تقديم محرك خطي متزامن أحادي الجانب في هذه الورقة مصمماً بمغناطيس مثبت على السطح بوجود اللف المتمركز وتمثله طبقاً لصيغ الدفع التحليلي مستندة على تأثيرات المتغيرات الهندسية مثل، تشكيلة احدود الملف، طول الفجوة الهوائية، وارتفاع المغناطيس الدائم. تبعاً لذلك، تم تنفيذ العديد من المنهجيات للتعامل مع هذه الظاهرة المؤدية. يتم انجاز تحليل الأداء ثنائي الأبعاد (D2) للنموذج المصمم والتحسين متعدد الأهداف الخاص به طريقة لتقليل قوة التجاذب المغناطيسي للمحرك باستخدام برنامج MAXWELL ANSYS. تُبين نتائج تصميم النموذج المثالي بأن النموذج الحاصل في قوة الدفع القصوى تقل بحوالي ٨١,٢٤ % مقارنة مع النموذج الأصلي (قبل التطوير) وبأصغر معامل تموج هو ٠,٢٢. أيضاً، تم أخذ خسائر القلب الحديدي بنظر الاعتبار وحالتين؛ القلب المرقق (ذو الشرائح) والقلب الصلب وفورنت النتائج في الحالتين. لقد وجد بأن خطأ نتائج التصميم بين الطرق التحليلية والعددية لحساب قوة الدفع الخارجة في المحرك لا تتجاوز ٠,٠٩٦٧.